LF Tracy: A Unified Single-Pipeline Approach for Salient Object Detection in Light Field Cameras

Fei Teng[1,2], Jiaming Zhang[3], Jiawei Liu[1,2], Kunyu Peng[3], Xina Cheng[4], Zhiyong Li[1,2,5], and Kailun Yang[1,2,*]

***Abstract*— Leveraging the rich information extracted from light field (LF) cameras is instrumental for dense prediction tasks. However, adapting light field data to enhance Salient Object Detection (SOD) still follows the traditional RGB methods and remains under-explored in the community. Previous approaches predominantly employ a custom two-stream design to discover the implicit angular feature within light field cameras, leading to significant information isolation between different LF representations. In this study, we propose an efficient paradigm (LF Tracy) to address this limitation. We eschew the conventional specialized fusion and decoder architecture for a dual-stream backbone in favor of a unified, single-pipeline approach. This comprises firstly a simple yet effective data augmentation strategy called MixLD to bridge the connection of spatial, depth, and implicit angular information under different LF representations. A highly efficient information aggregation (IA) module is then introduced to boost asymmetric feature-wise information fusion. Owing to this innovative approach, our model surpasses the existing state-of-the-art methods, particularly demonstrating a 23% improvement over previous results on the latest large-scale PKU dataset. By utilizing only $28.9M$ parameters, the model achieves a 10% increase in accuracy with $\sim 3M$ additional parameters compared to its backbone using RGB images and an 86% rise to its backbone using LF images. The source code will be made publicly available at https://github.com/FeiBryantkit/LF-Tracy.**

I. INTRODUCTION

The objective of Salient Object Detection (SOD) lies in mimicking human visual attention mechanisms to accurately identify the most conspicuous objects or regions in a variety of visual contexts. In particular, SOD plays a dual role: it not only aids robots in discerning the most striking elements in visual scenarios but also plays a pivotal role in several subsequent processes, including detection [1] and dense prediction task [2], [3]. However, within the SOD community, the current 2D-based methods [4], [5] rely on the powerful feature extraction capabilities of Convolutional Neural Networks and Transformers, coupled with finely crafted decoders, to achieve impressive results. A rich array of 3D methods [6], [7] has been introduced to boost the results further, incorporating depth information to enhance accuracy by effectively fusing the RGB information with depth feature cues. Inspired by that, LF cameras have been introduced [8], which capture the depth and angular information. However, we have noticed two significant limitations in these works.

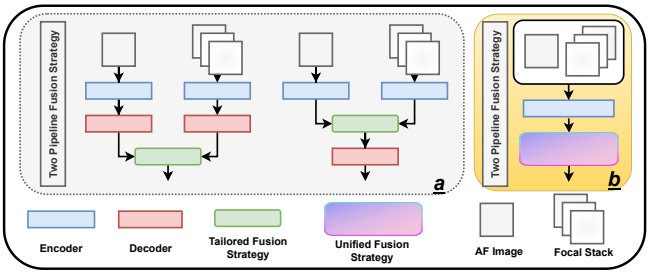

Fig. 1: Paradigms of LFSOD model. The conventional two-stream methods ($\underline{a}$) and our single-pipeline method ($\underline{b}$).

Limitation One: Lacking Pre-network Data Connectivity. Although researchers enhance the understanding of scenes in the LF community by introducing additional angular information, existing work on SOD for LF cameras still adheres to RGB-D fusion structures [9], [10] with traditional data augmentation strategies. This method isolatedly excavates the angular features and buries the relationship between different LF representations since there is no data interaction before the training process. Although a tolerated decoder is adopted to mitigate this issue, the loss of intrinsic relationship between various representations cannot be entirely compensated [11]. This motivates us to develop a novel strategy specifically for the LFSOD task to bridge a connection between various LF data sources before the training process.

Limitation Two: Lacking In-network Data Connectivity. The existing datasets for LF cameras consist of post-processed All-Focused (AF) images and Focal Stacks (FS). The asymmetric data construction introduced significantly enriches the geometric information captured by LF cameras. This includes depth, spatial information, and additional, implicit angular information derived from the interplay between images. While effectively utilizing depth and spatial information within separate images, the current two-stream approach (Fig. 1(a)) overlooks the vital connections between different images and the implicit angular information flow within the network. Moreover, relying solely on a single-pipeline

[1]F. Teng, J. Liu, Z. Li, and K. Yang are with the School of Robotics, Hunan University, China.
[2]F. Teng, J. Liu, Z. Li, and K. Yang are also with the National Engineering Research Center of Robot Visual Perception and Control Technology, Hunan University, China.
[3]J. Zhang and K. Peng are with the Institute for Robotics and Anthropomatics, Karlsruhe Institute of Technology, Germany.
[4]X. Cheng is with the School of Artificial Intelligence, Xidian University, China.
[5]Z. Li is also with the College of Computer Science and Electronic Engineering, Hunan University, China.
*Corresponding author: Kailun Yang (E-Mail: kailun.yang@hnu.edu.cn).

architecture for feature extraction from these images might result in sub-optimal results [12]. This is because merging the unfocused segments with all-focused data in FS images can lead to feature contamination. This process significantly impairs the discriminative capacity of the network, hindering its ability to identify and segment salient objects.

In this work, we propose a novel approach to overcome the aforementioned challenges. Firstly, a single-pipeline framework (LF Tracy) in Fig. 1(b) is established to achieve the in-network data connectivity. By learning different LF representations from a comprehensive perspective through a single backbone, our network can fully utilize the spatial, depth, and implicit angular information in LF images rather than conducting separate feature extraction for different representations. Furthermore, to effectively align and fuse the coupled features through the same backbone, a simple yet IA model is performed within LF Tracy. Moreover, a simple data augmentation strategy called MixLD is introduced to establish the pre-network data connectivity between different LF representations. Due to the highly efficient mechanism (MixLD+Backbone+IA), our network utilizes an additional $\sim 3M$ parameters, achieving a 10% performance improvement relative to the backbone using a single RGB image and an 86% performance improvement relative to the backbone with LF images. To demonstrate the high efficiency of the proposed approach, we perform comprehensive experiments on both a set of traditional LFSOD datasets [13], [14], [15] and the large-scale PKU dataset [16]. Experiment on the latest large-scale dataset, the PKU dataset, provides the best proof of the effectiveness of our method. By employing this mechanism, our network achieved a performance improvement of 23% relative to previous work.

At a glance, we deliver the following contributions:

- We propose a single-stream SOD paradigm, bridging the pre-network and in-network data connectivity.
- We design a low-parameter Information Aggregation (IA) Module that compensates for the inadequate feature learning of the single-branch network by filtering on a per-channel basis, and a data augmentation strategy, *i.e.*, MixLD, achieves pre-network data connectivity.
- Our method achieves top performance on three LF datasets and one large-scale PKU dataset with more than $10K$ images.

II. RELATED WORK

In real-world applications, LF cameras extend spatial coordinates with light direction beyond the RGB camera. Levoy *et al*. [17] introduced a two-plane parameterization to represent the imaging systems. This led to Ng *et al*. [18] inventing the light field camera, capable of capturing not only spatial context but also high-dimensional information through the angular domain. In this task, the discovery and connection of the high dimensional information of LF are crucial challenges to establishing an efficient SOD network. For that reason, this section will be divided into two parts: **Channel-wise Data Interation** in Sec. II-A and **Feature-wise Information Aggregation** in Sec. II-B.

A. Channel-wise Data Interaction

Light field cameras, which are equipped with several micro-lens, are capable of capturing angular information. FS images can be conducted using a certain image plane during the refocus procedure. The image plane is selected when adjusting the depth setting of each pixel. Since implicit angular information is concealed within combinations of multiple images and is unattainable through analysis of a single image, channel-wise data communication becomes essential for data preparation. However, research in this area remains unexplored. The traditional data augmentation strategies can be roughly divided into five categories based on the adjusted purpose. 1) Flipping the image along its vertical and horizontal axis is a typical technique to increase the diversity of data available for training. Furthermore, the rotation of an image with a certain angle also contributes. 2) Color jitter simulates images under different lighting and camera settings, enabling the trained model to better adapt to various scenarios. 3) Cutout [19] and Random Erasing [20] are introduced to drought or mismatch part of pixel-level information between neighboring pixels to increase the discrimination capability of the network. 4) Beyond deep learning, several works [21], [22] introduced machine learning-based strategies to boost the network capability. 5) Mixing-based methods [11], [23] leverage information from multiple images by generating input images that are blended.

Although those methods demonstrate the noticeable performance for a single image in the data augmentation community, the specific strategy designed for the combination of FS and AF images is also empty. Therefore, we introduce an efficient MixLD strategy to achieve channel-wise blending between asymmetric representations for SOD. It reconnected the images with different processing processes and boosted the network capability.

B. Feature-wise Information Aggregation

The inception of SOD can be traced back to rule-based methodologies, which predominantly relied on visual attributes such as color, contrast, and spatial distribution to ascertain salient areas in images [24], [25]. In recent years, there has been a paradigm shift in the SOD community towards leveraging deep learning paradigms, particularly convolutional neural networks. Specifically, MENet [26] introduced the iterative refinement and frequency decomposition mechanisms to improve detection accuracy significantly. By utilizing shared transformers and multi-scale refinement architectures, Wang *et al*. [27] decomposed into high-resolution and low-resolution images to achieve SOD. Furthermore, Zhang *et al*. [28] implemented SOD for panoramic images. Apart from those single-model SOD networks, depth prompts are introduced [6] to boost the performance, whereas several tasks [7], [29] adopted multi-model fusion between RGB and thermal information.

For the SOD task of LF, Wang *et al*. [30] implemented a convolutional neural network in the SOD community. Since then, the two-stream pipeline approach [12] for processing LF images has stood in a leading position in the field.

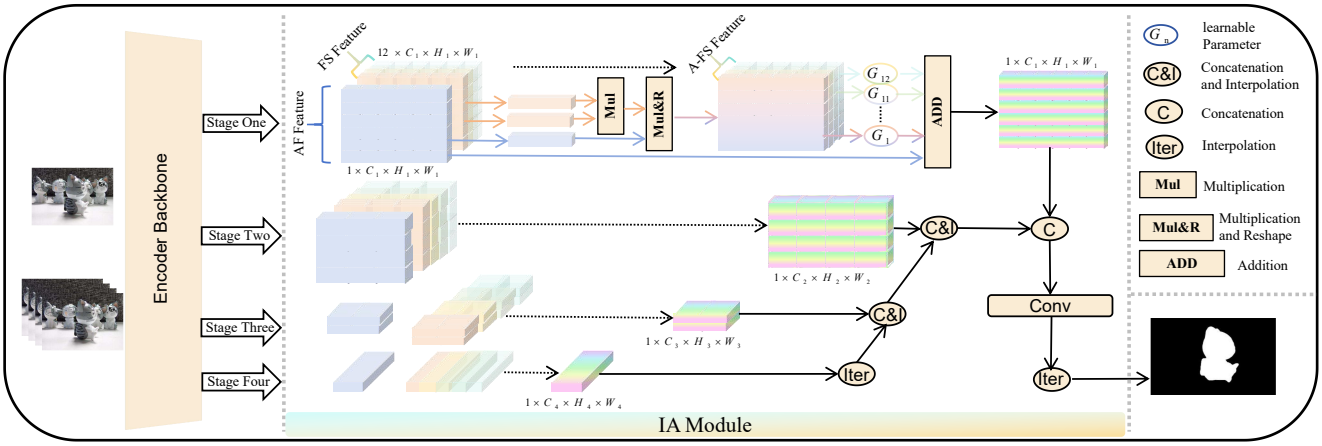

Fig. 2: Pipeline of LF Tracy network. FS and AS images are input into the backbone for feature extraction. Multi-level features are then fed into the IA module (Sec. III-C) for in-network data fusion and to predict the final result image.

Typically, this involves employing one backbone network for processing AF images and another for FS images or one depth image extracted from LF sub-aperture images. Although the two-stream pipeline approach has seen considerable advancement in not only SOD tasks but also semantic segmentation tasks [31], it is typically applied to modalities that are isolated, such as depth and RGB images. It is not suitable for LFSOD tasks based on AF and LF images.

For light field cameras, the depth, angular, and spatial information are embedded across different representations, *i.e.*, AF images and LF images. Processing these images in an isolated manner with a two-stream approach buries the angular features of light field cameras, and thus remains a sub-optimal method [11]. Therefore, our research is pivoting towards exploring a single-stream approach, allowing the network to learn different LF representations holistically.

III. METHOD

This section provides a comprehensive overview of our proposed paradigm, designed explicitly for LFSOD. Sec III-A delves into our innovative Data Augmentation Strategy. The intricate architecture of the framework is meticulously expounded in Sec III-B. Additionally, in Sec III-C, we introduce an advanced fusion module (IA module), which is pivotal for efficiently aggregating Light Field features.

A. Proposed LF Tracy Framework

As shown in Fig. 2, the proposed network has two components: a four-stage encoder providing rich multi-dimensional spatial information from different asymmetric data and the IA Module. The IA Module serves a dual purpose: 1) It overcomes the mismatching between the features established in-network connectivity through the same encoder block. 2) It can realign these features before sending them to the prediction head. To provide a more intuitive description of the information flow and interaction process, the AFttention image I^m_{AF} and FSttention stack I^m_{FS} are described separately. AFttention image and FSttention stack indicate the data source after MixLD. Furthermore, for simplicity, the following description is based on the stage one, which is the same for the other three stages. Especially, by applying the encoder block, the images are transferred into AF features $\{F_{AF} \in \mathbb{R}^{(64\times64\times64)}\}$ and FS features $\{F^n_{FS} \in \mathbb{R}^{(64\times64\times64)} | n \in [1, 12]\}$. After applying the IA Module, the 13 features are aggregated into one feature $\{f_1 \in \mathbb{R}^{(64\times64\times64)}\}$, which contains all spatial, angular, and depth information. After four stages, there is a set of feature maps $\{f_l | l \in [1, 4]\}$ with channel dimension $\{64, 128, 320, 512\}$. Meanwhile, at the training stage, to cooperate with the structure loss [32] calculation, f_l is also passed through one convolutional layer to compress channel information, as in Eq. (1).

$$f_{M_l} = Conv(64, 1)(f_l), \tag{1}$$

where $Conv(64, 1)(\cdot)$ convolutional layer with input channel 64 and output channel one and f_{M_l} denotes the feature after merging. Furthermore, drawing upon the structure loss $loss_{Str}$ as outlined in [33], we have integrated Tversky Loss $loss_T$ [34] into our training process. This integration aims to improve supervision during training, specifically targeting a reduction in false positives and false negatives.

B. Data Augmentation Strategy: MixLD

As depicted in Fig. 3, the primary objective of the specific data augmentation strategy for the LFSOD task is to amalgamate two distinct representations inherent in light field camera, namely, AF image I_{AF} and FS $\{I^n_{FS} | n \in [1, 12]\}$. This strategy is methodically partitioned into two discrete phases, each targeting specific aspects of the integration process. Initially, a non-intrusive approach is employed to integrate angular and depth information into the composite AF image while preserving the integrity of spatial data dimensions. Specifically, the data augmentation strategy can be described as following steps:

Firstly: Following the FS setting [35], one FS slice I^n_{FS} with dimension $\{3\times256\times256\}$ is randomly selected with a likelihood of 0.1. This FS image is then subjected to a pixel-level fusion process, meticulously blending it into the AF

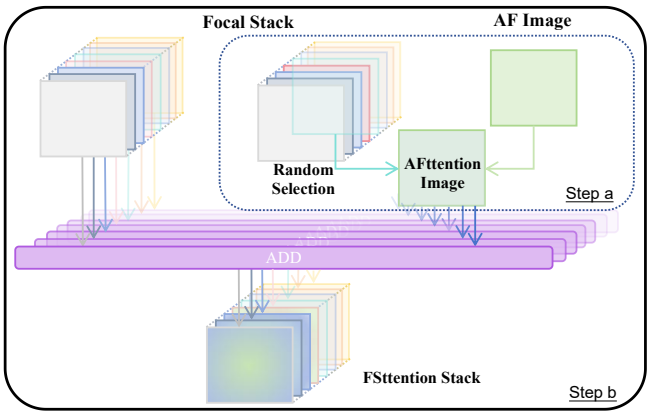

Fig. 3: Schematic illustration of our proposed MixLD strategy tailored for LFSOD. The strategy contains two independent steps (*a* and *b*), each of which is carried out randomly.

image representation, as shown in Eq. (2).

$$I_{AF}^{m} = \{\alpha \times I_{AF} + (1-\alpha)\{\text{Rand}(I_{FS}^{n})\}, \tag{2}$$

where α denotes the degree of blending and n indicates the quantities of focal images. I_{AF}^{m} indicates the AF image after blending, *i.e.*, AFttention image. In MixLD, α=1 indicates no blending and α=0 indicates that the AF Image is completely replaced. Only the AF image is altered during this process, while the FS images remain unchanged. Meanwhile, this procedure is not conducted for each interaction.

Secondly: The AFttention image is integrated into all the FS images with a probability of 0.5, as in Eq. (3).

$$I_{F_n}^{m} = \{\beta \times I_{AF}^{m} + (1-\beta) \times I_{FS}^{n}\}, \tag{3}$$

where β denotes also a super parameter for the degree of blending in stage two and n denotes the quantities of focal images. $I_{F_n}^{m}$ indicates the FS after blending *i.e.*, FSttention stack. This integration carried out with a fusion probability of 0.5 instead of 0.1, aims to make it more possible to enrich the FS with additional information. By blending the AF image into the FS images, each focal image retains its inherent depth-of-field information, gains implicit angular insights from the other focal image, and enhances its spatial richness with the detailed information from the AF image. Furthermore, the AFttention image I_{AF}^{m} and FSttention stack $\{I_{F_n}^{m} | n \in [1, 12]\}$ are fed into the network. It is important to emphasize that not each stage is executed as a matter of course.

It is precisely through this form of blending that the neural network while learning the inherent AF and FS information, can break out of the conventional framework to learn implicit angular information.

C. Information Aggregation: IA Module

To fuse the implicit angular, explicit spatial, and depth information from asymmetric data, we introduce a simple IA Module that follows a two-step interaction process. Given single feature $\{F_{FS}^{n} | n \in [1, 12]\}$, the FS-guided Querry and Key are generated through their respective convolutional layer. Through matrix multiplication, the attention map $\{M \in \mathbb{R}^{(4096\times4096)}\}$ is obtained. In this step, the attention map integrates a broader context into the aggregation of local features and enhances the representative capability of the focus part. Furthermore, applying the third convolutional layer to F_{AF}, the AF image guided Value $\{V_{AF} \in \mathbb{R}^{4096\times8}\}$ is generated, as in Eq. (4)-(7).

$$Q = Conv_q(C_{in}, C_{out})(F_{FS}^{n}), \tag{4}$$
$$K = Conv_k(C_{in}, C_{out})(F_{FS}^{n}), \tag{5}$$
$$M = Soft\{Mul(Q, K)\}, \tag{6}$$
$$V = Conv_v(C_{in}, C_{out})(F_{AF}). \tag{7}$$

The tokens $\{T \in \mathbb{R}^{4096\times8}\}$, which contains information from certain focal images, is obtained by multiplication of attention map and Value, as in Eq. (8).

$$T = Mul(M, V). \tag{8}$$

After obtaining the tokens, the A-FS features $\hat{F}_{FS}^{n}$ are generated by applying the reshape operation. Note that the number of images has remained unchanged until now. This operation aims to enhance the spatial information at the corresponding depth by guiding the information from the FS image and, with the help of AF features, establish a connection between the global AF and FS information. Additionally, we introduce a set of leanable parameters to calculate the contribution of different FS features. To further enhance the spatial context information, a submission is undertaken, and the final result f_1 is obtained as in Eq. (9).

$$f_1 = AF + \sum_{i=1}^{12} \sigma \times \hat{F}_{FS}^{n}. \tag{9}$$

Given multi-scale features $\{f_1, f_2, f_3, f_4\}$, the interpolation and concatenation are conducted to aggregate the features. Applying the convolutional layer following an interpolation, the mask f is compressed and sent to the prediction head.

IV. EXPERIMENTS

To effectively demonstrate the efficacy of our approach, we showcase the quantitative result and qualitative results on different datasets. Firstly, we introduce our experimental setup in Sec. IV-A. In Sec. IV-B, we present a quantitative comparison with other methods. Additionally, in Sec. IV-C, we showcase the visual results of our method, along with a visual comparison with previous approaches.

A. Implementation Details

Datasets: The experiences are conducted in traditional LFSOD datasets, which include LFSD [13], DUT-LF [14], HFUT [15] and a large-scale PKU dataset [16]. Especially, two experiment strategies are conducted: **I)** training on DUT-LF + HFUT, ∼1000 images, and evaluation on the whole LFSD dataset, the DUT-LF testing dataset, and HFUT testing dataset; **II)** training and testing on the PKU-LF dataset. PKU-LF dataset contains more than $10K$ images. For the ablation study, the experiments are based on experiment strategy one.

Methods	LFS [13]	WSC [36]	DILF [37]	MoLF [14]	ERNet [38]	BBS [39]	JLDCF [40]	SSF [41]	UCNet [42]	D3Net [43]	S2MA [44]	cmMS [45]	HDF [46]	ATSA [47]	MINet [4]	GCPA [5]	$STSA_1$ [16]	$STSA_2$ [16]	$STSA_3$ [16]	**Ours**	**Gain**
LFSD	.205	.150	.136	.088	.082	.072	.070	.067	.072	.095	.094	.073	.086	.068	.096	.093	.067	.065	.062	.046	30%
HFUT	.221	.154	.150	.094	.082	.089	.075	.100	.090	.091	.112	.097	.095	.084	.088	.094	.067	.072	.057	.056	02%
DUT-LF	.227	.149	.165	.051	.039	.066	.058	.050	.081	.083	.102	.079	.091	.041	.060	.061	.033	.030	.027	.023	17%
PKU-LF	.214	.132	.143	.066	.059	.056	.049	.052	.070	.067	.100	.052	.065	.045	.050	.055	.047	.042	.035	.027	23%

TABLE I: Quantitative comparison with other methods on different datasets in terms of MAE. The best result is highlighted in red. "Gain" indicates the improvement in our results compared to previous state-of-the-art methods in percentage. $STSA_1$, $STSA_2$, and $STSA_3$ represent the outcomes of the PKU Team [16] using different quantities of data for training.

Dataset	Metrics	PreV	Our	Gain
LFSD [13]	F_β^{mean}	.862	.896	+3.9%
	E_β^{mean}	.902	.912	+1.2%
	S_α	.871	.902	+3.5%
HFUT [15]	F_β^{mean}	.771	.769	-0.2%
	E_β^{mean}	.864	.865	+0.1%
	S_α	.834	.833	-0.1%
DUT-LF [14]	F_β^{mean}	.906	.936	+3.3%
	E_β^{mean}	.954	.957	+0.3%
	S_α	.928	.938	+1.1%

TABLE II: Quantitative comparison with other methods on different datasets in terms of F_β^{mean}, E_β^{mean}, and S_α. We conduct an unequal comparison by selecting the highest results from previous works *i.e.*, "PreV" and comparing them with our results.

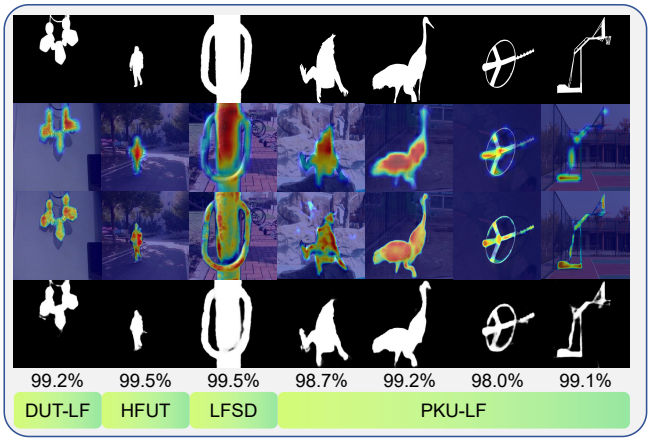

Fig. 4: Qualitative Result on four datasets. From top to bottom, the ground truth, AF image feature maps, decoder maps, and predicted masks are illustrated.

Setting Details: The image size for all the datasets is 256×256. Each scene is structured to contain exactly 12 focal slices to meet specific coding requirements. This is achieved by strategically duplicating focal slices in the original order, ensuring that the duplication process maintains the original sequence of the slices. Data augmentation is applied with Flipping, Cropping, Rotating, and MixLD for the training process. The blending parameter α, β are set into 0.5 and 0.5, respectively. The AdamW optimizer with a learning rate of $5e^{-5}$ and weight decay of $1e^{-4}$ is adapted for training. All the experiments are adapted to a single A6000 GPU with a batch size of 6. The training epochs are limited to 300, and the encoder conducts PVTv2 [48].

Evaluation Metrics: To analyze the results of different methods, we employ mean absolute error (MAE) [49] for a fair comparison. And since F-measure (F_β^{mean}) [50], E-measure (S_β^{man}) [32], S-measure (S_α) rely on multiple thresholds, we choose them based on training strategy one for an unfair comparison, to highlight the accuracy of our method. Specifically, we select the best results from all previous experiments to compare with ours.

B. Quantitative Results

To verify our approach, we compare the designed network with existing methods and demonstrate the superiority of our approach. Table I shows that the best performance of our proposed approach significantly outperforms existing methods across the LFSD series dataset and PKU dataset on MAE. Due to the variability in performance across different evaluation metrics and datasets, we follow the benchmark provided by the PKU team [16]. Specifically for the STSA metric, we have selected the best result from the available experiments, which entails using an expanded training set ($STSA_3$). Our proposed method significantly surpasses this integrated benchmark. The network's performance is most effectively proved, particularly with the large-scale and richly varied PKU dataset. By establishing the pre-network connectivity and the in-network connectivity of LF data, our network reconnects the intrinsic relationships between different light field camera images, achieving a 23% improvement in MAE compared with $STSA_3$. It should be noted that the training dataset of $STSA_3$ is an extension dataset (DUT-LF + HFUT + PKU-LF). In Table IV, we perform a biased comparison in terms of other evaluation criteria, choosing the highest results from prior research for contrast against our results.

C. Qualitative Results

It can be seen from Fig. 4 that our network achieves outstanding accuracy across different scenarios by establishing pre-network and in-network connectivity. Whether dealing

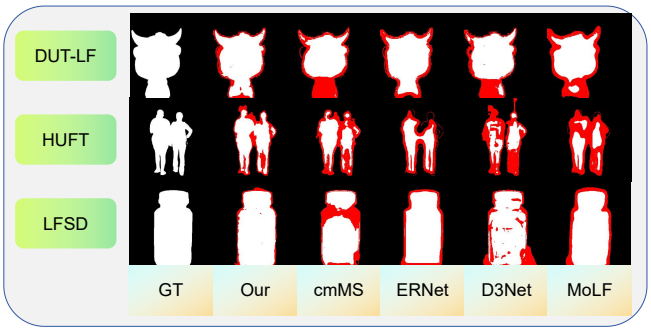

Fig. 5: Qualitative Comparison on three datasets. The difference maps between the visual results of various methods and the ground truth are displayed. Red pixels indicate pixels where the predicted results do not align with the ground truth.

with a single scene, some complex scenarios, or simple to complex structures, our network also delivers excellent visualization results. Especially, for transparent backboards under varying lighting conditions, our network identifies the object through efficient information processing. Furthermore, the results of the visual comparison vividly demonstrate the superiority of our method, as in Fig. 5. Our network accurately identifies the locations of objects, and notably, it precisely differentiates challenging boundaries and lines. For the images in the middle row, the area with two pedestrians walking side by side is particularly challenging to discern. The varied colors and textures of their clothing present a significant challenge to the network. While other methods show numerous errors in this region, our network achieves accurate differentiation.

V. ABLATION STUDIES

In this section, several ablation studies are conducted to discuss the effectiveness of our proposed methods and the selection of super-parameters and backbones. Firstly, in Sec. V-A, the experiments are carried out to comprehensively examine the effects of various components incorporated in our methods. Sec. V-B demonstrated the impact of the blending rates in MixLD on performance. Sec. V-C explores the effects of the quantity of FS images on performance. Sec. V-D investigates the performance of different backbones on the task of SOD.

A. Ablation Study for the Approach

In our experimental analysis, as shown in Table III, we ablated components of our approach to assess their contributions. The optimal performance achieved an MAE of 0.046. Firstly, eliminating our data augmentation strategy MixLD resulted in a performance decrease, and adapting CutMib [11] has few contributions to the performance. This indicates the necessity of MixLD for connecting the different data before sending them into the network. After that, we ablate the core component of our network, the IA module, and the MAE dramatically increased. The observed significant disparity of 0.286 markedly illustrates the critical role of our IA module in the overall framework. This module

Model	Our	wo. MixLD	w. CutMib	wo. IA	wo. LF
MAE	.046	.052	.051	.332	.057

TABLE III: Ablation Study of LF Tracy network. The best result is highlighted in red. "wo." is the abbreviation for "without" and "w." is the abbreviation for "with". We also include a comparison with "CutMib" [11].

$\alpha = \beta$	1	3	5	7	9
MAE	.053	.049	.046	.073	.142

TABLE IV: Exploration of the blending rates in MixLD. The rates α and β remain the same. The best result is colored in red. Five blending rates are adopted in this step.

is integral for effectively realigning and managing the data imbalance across diverse sources. In particular, it is pivotal in reducing data mismatching between LF and AF images, facilitating more effective data integration, and improving accuracy with only one stream encoder. Finally, without FS, the result is further reduced.

Stack Size	2	3	5	12
wo. IA	.137	.141	.205	.332
w. IA	.051	.051	.049	.046

TABLE V: Investigating the impact of varying quantities of FS mages on MAE. "wo." is the abbreviation for "without" and "w." is the abbreviation for "with". The best result is highlighted in red.

Backbone	B0	B1	B2	B4
PVTv2 [48]	.120	.097	.072	.087
AgentPVT [51]	.153	.137	.142	.145

TABLE VI: Analysis of the network performance through different backbones. The best result is highlighted in red. MAE are reported.

B. Ablation Study for the Blending Rate in MixLD

To explore the optimal blending ratio of AF image and FS. We altered the parameter α in the first step, which involves blending one FS slice into AF images. Furthermore, in the second step, the parameter β is adjusted to merge the blended AF image into FS. Due to the various combinations of $\alpha - \beta$ paar, we only experimented with a few combinations based on $\alpha = \beta$. As demonstrated in Table IV, the optimal outcome is achieved with a blending rate of 0.5. Notably, deviations from this ratio, either by increasing or decreasing the blending rate, result in a discernible decline in the network's performance.

C. Ablation Study for the IA Module

To demonstrate the alignment and fusion capabilities of our IA module for asymmetric data, we compared the discrimination ability of the network with and without the IA module, using 2, 3, 5, and 12 FS images, respectively. As indicated in Table V, without the IA module, continuously stacking FS images does not enhance the network's capability; rather, it negatively impacts the network. However, with the addition of the IA module, the focused range and implicit angular information in the FS are utilized, leading to a continuous increase in the network's discrimination ability.

D. Selection of Various Backbone

We conducted a series of experiments based on traditional datasets to assess the optimal feature extraction methods. Initially, we experimented with the PVTv2 network [48] as the backbone. After that, we explored the recently proposed AgentFormer [51] based PVTv2 framework. To prevent pre-trained weights from causing an unfair comparison in our selection of methods, we conducted experiments for 100 epochs without pre-trained weights. Table VI shows that the agent attention method is not suitable for our dataset, and the experimental results on the LFSOD dataset do not improve with the increase in the number of parameters. Due to this reason, we have chosen PVTv2 as the backbone.

VI. CONCLUSION

Contribution: In our paper, we present a unified single-stream method for salient object detection, outperforming the conventional two-stream approach with state-of-the-art results. *Firstly:* We propose a data augmentation strategy for saliency object detection, specifically targeting the pre-network connectivity. This method facilitates interaction among different channels of data, enhancing the network's discriminative ability. *Secondly*: we have designed an efficient IA module. This module effectively addresses the feature mismatching of different LF representations and enables in-network data connectivity under a single pipeline network. Uniquely, our study tested the network's performance and achieved leading results on two distinct datasets concurrently.

Limitation and Further Work: The heterogeneity in image representation methods precludes a comprehensive evaluation of the network's performance. To address this, our future work will consolidate existing datasets into a cohesive framework. This will enable the community to conduct a more precise evaluation of network capabilities. Meanwhile, we aim to advance the development of light field camera perception by reducing the complexity of light field camera networks while preserving their ability to capture multi-dimensional features.

REFERENCES

[1] R. B. Girshick, J. Donahue, T. Darrell, and J. Malik, "Rich feature hierarchies for accurate object detection and semantic segmentation," in *Proc. CVPR*, 2013.

[2] W. Wang, J. Shen, and F. Porikli, "Saliency-aware geodesic video object segmentation," in *Proc. CVPR*, 2015.

[3] A. Borji and L. Itti, "State-of-the-art in visual attention modeling," *IEEE Transactions on Pattern Analysis and Machine Intelligence*, 2013.

[4] Y. Pang, X. Zhao, L. Zhang, and H. Lu, "Multi-scale interactive network for salient object detection," in *Proc. CVPR*, 2020.

[5] Z. Chen, Q. Xu, R. Cong, and Q. Huang, "Global context-aware progressive aggregation network for salient object detection," in *Proc. AAAI*, 2020.

[6] F. Sun, P. Ren, B. Yin, F. Wang, and H. Li, "CATNet: A cascaded and aggregated transformer network for RGB-D salient object detection," *IEEE Transactions on Multimedia*, 2023.

[7] G. Chen *et al.*, "Modality-induced transfer-fusion network for RGB-D and RGB-T salient object detection," *IEEE Transactions on Circuits and Systems for Video Technology*, 2022.

[8] T. Georgiev and C. Intwala, "Light field camera design for integral view photography," *Adobe System, Inc., Technical Report*, 2006.

[9] Y. Chen, G. Li, P. An, Z. Liu, X. Huang, and Q. Wu, "Light field salient object detection with sparse views via complementary and discriminative interaction network," *IEEE Transactions on Circuits and Systems for Video Technology*, 2023.

[10] G. Chen *et al.*, "Fusion-embedding siamese network for light field salient object detection," *IEEE Transactions on Multimedia*, 2023.

[11] Z. Xiao, Y. Liu, R. Gao, and Z. Xiong, "CutMIB: Boosting light field super-resolution via multi-view image blending," in *Proc. CVPR*, 2023.

[12] D. Jing, S. Zhang, R. Cong, and Y. Lin, "Occlusion-aware bi-directional guided network for light field salient object detection," in *Proc. MM*, 2021.

[13] N. Li, J. Ye, Y. Ji, H. Ling, and J. Yu, "Saliency detection on light field," in *Proc. CVPR*, 2014.

[14] M. Zhang, J. Li, J. Wei, Y. Piao, and H. Lu, "Memory-oriented decoder for light field salient object detection," in *Proc. NeurIPS*, 2019.

[15] J. Zhang, M. Wang, L. Lin, X. Yang, J. Gao, and Y. Rui, "Saliency detection on light field: A multi-cue approach," *ACM Transactions on Multimedia Computing, Communications, and Applications (TOMM)*, 2017.

[16] W. Gao, S. Fan, G. Li, and W. Lin, "A thorough benchmark and a new model for light field saliency detection," *IEEE Transactions on Pattern Analysis and Machine Intelligence*, 2023.

[17] M. Levoy and P. Hanrahan, "Light field rendering," in *Seminal Graphics Papers: Pushing the Boundaries*, 2023.

[18] R. Ng, *Digital light field photography*. Stanford University, 2006.

[19] T. DeVries and G. W. Taylor, "Improved regularization of convolutional neural networks with cutout," *arXiv preprint arXiv:1708.04552*, 2017.

[20] Z. Zhong, L. Zheng, G. Kang, S. Li, and Y. Yang, "Random erasing data augmentation," in *Proc. AAAI*, 2020.

[21] B. Ekin, V. Dandelion, and Q. V. Le, "AutoAugment: Learning augmentation policies from data," in *Proc. CVPR*, 2019.

[22] C. Zhang, X. Li, Z. Zhang, J. Cui, and B. Yang, "BO-Aug: learning data augmentation policies via bayesian optimization," *Applied Intelligence*, 2023.

[23] C. Florea, C. Vertan, and L. Florea, "SoftClusterMix: Learning soft boundaries for empirical risk minimization," *Neural Computing and Applications*, 2023.

[24] L. Itti, C. Koch, and E. Niebur, "A model of saliency-based visual attention for rapid scene analysis," *IEEE Transactions on Pattern Analysis and Machine Intelligence*, 1998.

[25] R. Achanta, F. Estrada, P. Wils, and S. Süsstrunk, "Salient region detection and segmentation," in *Proc. ICVS*, 2008.

[26] Y. Wang, R. Wang, X. Fan, T. Wang, and X. He, "Pixels, regions, and objects: Multiple enhancement for salient object detection," in *Proc. CVPR*, 2023.

[27] X. Deng, P. Zhang, W. Liu, and H. Lu, "Recurrent multi-scale transformer for high-resolution salient object detection," in *Proc. MM*, 2023.

[28] R. Cong, K. Huang, J. Lei, Y. Zhao, Q. Huang, and S. Kwong, "Multi-projection fusion and refinement network for salient object detection in 360° omnidirectional image," *IEEE Transactions on Neural Networks and Learning Systems*, 2023.

[29] R. Cong *et al.*, "Does thermal really always matter for RGB-T salient object detection?" *IEEE Transactions on Multimedia*, 2023.

[30] T. Wang, Y. Piao, X. Li, and H. Lu, "Deep learning for light field saliency detection," in *Proc. ICCV*, 2019.

[31] J. Zhang *et al.*, "Delivering arbitrary-modal semantic segmentation," in *Proc. CVPR*, 2023.

[32] D.-P. Fan, M.-M. Cheng, Y. Liu, T. Li, and A. Borji, "Structure-measure: A new way to evaluate foreground maps," in *Proc. ICCV*, 2017.

[33] J. Wei, S. Wang, and Q. Huang, "F^3Net: Fusion, feedback and focus for salient object detection," in *Proc. AAAI*, 2020.

[34] S. Salehi, D. Erdogmus, and A. Gholipour, "Tversky loss function for image segmentation using 3D fully convolutional deep networks," in *Proc. MLMI@MICCAI*, 2017.

[35] Y. Piao, Y. Jiang, M. Zhang, J. Wang, and H. Lu, "PANet: Patch-aware network for light field salient object detection," *IEEE Transactions on Cybernetics*, 2023.

[36] N. Li, B. Sun, and J. Yu, "A weighted sparse coding framework for saliency detection," in *Proc. CVPR*, 2015.

[37] J. Zhang, M. Wang, J. Gao, Y. Wang, X. Zhang, and X. Wu, "Saliency detection with a deeper investigation of light field." in *Proc. IJCAI*, 2015.

[38] Y. Piao, Z. Rong, M. Zhang, and H. Lu, "Exploit and replace: An asymmetrical two-stream architecture for versatile light field saliency detection," in *Proc. AAAI*, 2020.

[39] D.-P. Fan, Y. Zhai, A. Borji, J. Yang, and L. Shao, "BBS-Net: RGB-D salient object detection with a bifurcated backbone strategy network," in *Proc. ECCV*, 2020.

[40] K. Fu, D.-P. Fan, G.-P. Ji, Q. Zhao, J. Shen, and C. Zhu, "Siamese network for RGB-D salient object detection and beyond," *IEEE Transactions on Pattern Analysis and Machine Intelligence*, 2022.

[41] M. Zhang, W. Ren, Y. Piao, Z. Rong, and H. Lu, "Select, supplement and focus for RGB-D saliency detection," in *Proc. CVPR*, 2020.

[42] J. Zhang *et al.*, "Uncertainty inspired RGB-D saliency detection," *IEEE Transactions on Pattern Analysis and Machine Intelligence*, 2021.

[43] D.-P. Fan, Z. Lin, Z. Zhang, M. Zhu, and M.-M. Cheng, "Rethinking RGB-D salient object detection: Models, data sets, and large-scale benchmarks," *IEEE Transactions on Neural Networks and Learning Systems*, 2021.

[44] N. Liu, N. Zhang, and J. Han, "Learning selective self-mutual attention for RGB-D saliency detection," in *Proc. CVPR*, 2020.

[45] C. Li, R. Cong, Y. Piao, Q. Xu, and C. C. Loy, "RGB-D salient object detection with cross-modality modulation and selection," in *Proc. ECCV*, 2020.

[46] Y. Pang, L. Zhang, X. Zhao, and H. Lu, "Hierarchical dynamic filtering network for RGB-D salient object detection," in *Proc. ECCV*, 2020.

[47] M. Zhang, S. X. Fei, J. Liu, S. Xu, Y. Piao, and H. Lu, "Asymmetric two-stream architecture for accurate RGB-D saliency detection," in *Proc. ECCV*, 2020.

[48] W. Wang *et al.*, "PVT v2: Improved baselines with pyramid vision transformer," *Computational Visual Media*, 2022.

[49] F. Perazzi, P. Krähenbühl, Y. Pritch, and A. Hornung, "Saliency filters: Contrast based filtering for salient region detection," in *Proc. CVPR*, 2012.

[50] R. Achanta, S. Hemami, F. Estrada, and S. Susstrunk, "Frequency-tuned salient region detection," in *Proc. CVPR*, 2009.

[51] Y. Yuan, X. Weng, Y. Ou, and K. M. Kitani, "AgentFormer: Agent-aware transformers for socio-temporal multi-agent forecasting," in *Proc. ICCV*, 2021.